

Effect of electrons scattered by optical phonons on superconductivity in $M\text{H}_3$ ($M = \text{S}, \text{Ti}, \text{V}, \text{Se}$)

Quan Zhuang, Xilian Jin,^{*} Tian Cui,^{*} Die Zhang, Ying Li, Xin Li, Kuo Bao, and Bingbing Liu
State Key Laboratory of Superhard Materials, College of Physics, Jilin University, Changchun 130012, China

 (Received 17 May 2018; revised manuscript received 25 June 2018; published 24 July 2018)

For exploring the superconductivity mechanisms and seeking potential high-temperature superconductors in hydrogen-rich compounds, we perform a systematical investigation of the phase diagram, crystal structures, electronic properties, and electron-phonon coupling (EPC) of titanium hydrides under high pressures. Strikingly, the low T_c in TiH_3 (~ 4 K) contrast sharply with the high T_c (above 200 K) in SH_3 , though they both possess the same stoichiometry and both crystallize in high-symmetrical cubic crystal. The large difference of T_c motivates us to discover the superconductive mechanism by probing the electron-phonon coupling interaction in the cubic crystal of SH_3 , TiH_3 , VH_3 , and SeH_3 . The analyses of phonon linewidths and Fermi surface nesting functions reveal that the contrasting T_c is mainly attributed to the disparate intensity of electrons interacting with optic phonons, rather than the contributions from global electronic structures. Furthermore, it is found that the strong dependency of optic phonon frequencies on the wave vector is an essential ingredient for strong EPC λ .

DOI: [10.1103/PhysRevB.98.024514](https://doi.org/10.1103/PhysRevB.98.024514)

I. INTRODUCTION

Looking for a room-temperature superconductor is one of biggest issues in the fields of science. Ashcroft suggested that the metallic phase of solid hydrogen has the potential to be a high-temperature superconductor [1]. The superconductivity has been predicted with high superconducting transition temperatures (T_c) in the range of room temperature theoretically [2–4]. Unfortunately, the experimental attempt up to 388 GPa has not yet realized the metallic solid hydrogen [5]. Recently, the metallization of solid hydrogen has been reported experimentally at an ultrahigh pressure of 495 GPa [6], but additional experimental measurements are recommended to verify this claim [7,8].

The idea of metallic superconducting hydrogen has been expanded into hydrogen-rich compounds owing to the “chemical precompression,” and these compounds can metallize at much lower pressures than the upper limit of current high-pressure techniques [9–16]. Among these studies, a high T_c above 200 K in H_3S was predicted by Duan *et al.* [16] and has been confirmed by subsequent works. An inspiring experimental breakthrough has been reported with the observation of T_c above 200 K in H_2S compressed to 200 GPa [17]. From the electronic structure and electron-phonon coupling (EPC) calculations [18–20] and x-ray diffraction experiments [21], the structure of the superconducting phase is shown to be consistent with the decomposed product H_3S with a cubic structure predicted theoretically [16]. Moreover, investigations of other hydrogen-dominated compounds have been stimulated by these breakthrough discoveries [22–29]. The transition-metal hydrides YH_6 [22], LaH_{10} , and YH_{10} [23,24] have been predicted to possess remarkably high- T_c values above 200 K. As to the group-IVB element Ti, the phase transition of TiH_2 has been explored experimentally and theoretically [30,31].

At ambient pressure, strong electron-phonon coupling with an estimated λ of 0.84 was predicted in TiH_2 [32]. However, the structures and superconductivity of other stoichiometries are barely reported under high pressures. This stimulated us to perform an investigation of titanium hydrides in order to search for feasible high-temperature superconductors and explore the superconductivity mechanism.

Herein, the phase diagram, crystal structures, electronic properties, and electron-phonon coupling of titanium hydrides are deeply investigated. Four species, namely, TiH , TiH_2 , TiH_3 , and TiH_6 , are found to be stable under high pressures. The structures and phase transitions in TiH_2 are consistent with those reported in previous studies. Conspicuously, the low T_c in TiH_3 (~ 4 K) contrast sharply with the high T_c (above 200 K) in SH_3 (H_3S can be written as SH_3), though they both possess the same stoichiometry and both crystallize in high-symmetrical cubic crystal. Then we probe the mechanism by comparing superconductivity in cubic SH_3 , TiH_3 , and SeH_3 [26], along with the low- T_c $Fm-3m$ (VH_3) that we predicted before [29]. As is expected, the tremendous difference of T_c arise from the disparate EPC parameter λ . Further analyses of phonon linewidths and the Fermi surface nesting function illustrated that the contributions from global electronic structures to the formation of the Cooper pair in the four compounds are similar, and thus they are not responsible for the contrasting λ . Hence, the disparate intensity of electrons interacting with optical branches is the dominator. Furthermore, the strong dependency feature of optic phonon frequencies on the wave vector is disclosed to be an essential ingredient for strong EPC λ and high T_c . We hope our findings are helpful to understand the superconductive mechanism in hydrogen-rich metals.

II. COMPUTATIONAL DETAILS

We determine the superconducting transition temperature (T_c) by utilizing the Allen-Dynes modified McMillan

^{*}Corresponding authors: jinxilian@jlu.edu.cn; cuitian@jlu.edu.cn

equation [33,34],

$$T_c = \frac{\omega_{\log}}{1.2} \exp\left[-\frac{1.04(1+\lambda)}{\lambda - \mu^*(1+0.62\lambda)}\right], \quad (1)$$

where μ^* is the Coulomb pseudopotential [35], λ is the EPC constant, and ω_{\log} is the logarithmic averaged frequency. The EPC λ can be obtained by the integral

$$\lambda = 2 \int_0^\infty \frac{\alpha^2 F(\omega)}{\omega} d\omega. \quad (2)$$

Other important frequency moments of $\alpha^2 F(\omega)$ are defined as [36]

$$\omega_{\log} = \exp\left[\frac{2}{\lambda} \int_0^\infty \frac{d\omega}{\omega} \alpha^2 F(\omega) \ln \omega\right] \quad (3)$$

and

$$\langle \omega^2 \rangle = \frac{2}{\lambda} \int_0^\infty \omega \alpha^2 F(\omega) d\omega, \quad (4)$$

where the parameter ω denotes the phonon frequency and $\alpha^2 F(\omega)$ is the Eliashberg spectral function [37]:

$$\alpha^2 F(\omega) = \frac{1}{2\pi N(\varepsilon_F)} \sum_{\mathbf{q}\nu} \frac{\gamma_{\mathbf{q}\nu}}{\omega_{\mathbf{q}\nu}} \delta(\omega - \omega_{\mathbf{q}\nu}). \quad (5)$$

The phonon wave vector is represented as \mathbf{q} , and the phonon frequency of the mode ν at \mathbf{q} is represented by $\omega_{\mathbf{q}\nu}$. The phonon linewidth $\gamma_{\mathbf{q}\nu}$ is given by

$$\gamma_{\mathbf{q}\nu} = \pi \omega_{\mathbf{q}\nu} \sum_{mn} \sum_{\mathbf{k}} |g_{mn}^{\nu}(\mathbf{k}, \mathbf{q})|^2 \delta(\varepsilon_{m,\mathbf{k}+\mathbf{q}} - \varepsilon_F) \times \delta(\varepsilon_{n,\mathbf{k}} - \varepsilon_F). \quad (6)$$

Here, the electron-phonon matrix element $g_{mn}^{\nu}(\mathbf{k}, \mathbf{q})$ for scattering an electron from state $|m, \mathbf{k} + \mathbf{q}\rangle$ to $|n, \mathbf{k}\rangle$ while emitting or absorbing a phonon $\mathbf{q}\nu$ with frequency ω is given by [38]

$$g_{mn}^{\nu}(\mathbf{k}, \mathbf{q}) = \left(\frac{\hbar}{2M\omega_{\mathbf{q}\nu}}\right)^{1/2} \langle m, \mathbf{k} + \mathbf{q} | \delta_{\mathbf{q}\nu} V_{\text{SCF}} | n, \mathbf{k} \rangle. \quad (7)$$

Here, $|n, \mathbf{k}\rangle$ is the bare electronic Bloch state, and $\delta_{\mathbf{q}\nu} V_{\text{SCF}}$ is the derivative of the self-consistent potential with respect to a collective ionic displacement corresponding to phonon wave vector \mathbf{q} and mode ν .

In terms of phonon linewidths, the overall EPC parameter λ can be expressed as

$$\lambda = \sum_{\mathbf{q}\nu} \lambda_{\mathbf{q}\nu} = \sum_{\mathbf{q}\nu} \frac{\gamma_{\mathbf{q}\nu}}{\pi N(\varepsilon_F) \omega_{\mathbf{q}\nu}^2}. \quad (8)$$

The in-house developed ELocR code is utilized to determine the preferred structures of titanium hydrides at high pressures [29,39]. The underlying *ab initio* structural relaxations and electronic properties are performed using density functional theory within the Perdew-Burke-Ernzerhof (PBE) of generalized gradient approximation (GGA) [40], as implemented in the Vienna *ab initio* simulation package (VASP 5.3.2) [41]. The GW pseudopotentials for H and Ti are adopted. The 1s cutoff radius is 0.8 a.u. for hydrogen. For titanium, the radius for 3s3p4s3d is 2.2 a.u. One and twelve electrons are treated

as valence for H and Ti, respectively. The plane-wave kinetic-energy cutoff of 1000 eV and appropriate Monkhost-Pack k meshes with grid spacing of $2\pi \times 0.025 \text{ \AA}^{-1}$ were adopted to ensure the convergence of the total-energy calculations.

Phonon and electron-phonon calculations of stable Ti-H compounds are carried out within the framework of the linear-response theory via the QUANTUM ESPRESSO package [42]. We employ Trouiller-Martins-type norm-conserving pseudopotentials for Ti and H [43]. Convergence tests provide a suitable value of 80 Ry kinetic-energy cutoff. The q -point mesh in the first Brillouin zone of $4 \times 4 \times 4$ for $I4/mmm$ (TiH), $7 \times 7 \times 5$ for $I4/mmm$ (TiH₂), $7 \times 7 \times 4$ for $P4/nmm$ (TiH₂), $4 \times 4 \times 4$ for $Fm-3m$ (TiH₃), $3 \times 4 \times 3$ for $Immm$ (TiH₆), $4 \times 4 \times 4$ for $Fm-3m$ (VH₃), and $4 \times 4 \times 4$ for $Im-3m$ (SH₃) are used for phonon and electron-phonon calculations. The zero-point energy (ZPE) is estimated as

$$E_{\text{ZPE}} = \left(\frac{1}{2}\right) \sum_{\mathbf{q}\nu} \hbar \omega_{\mathbf{q}\nu}, \quad (9)$$

where ν indicates a phonon branch at wave vector \mathbf{q} .

III. RESULTS AND DISCUSSIONS

We focus our variable-composition structure searches on hydrogen-rich compounds that are promising candidates for higher- T_c superconductors [9]. The thermodynamic stabilities of a variety of titanium hydrides are evaluated by their formation enthalpies relative to the products of dissociation into constituent elements at 0, 50, 100, 150, and 200 GPa, as summarized in the convex hull depicted in Fig. 1 and also in Fig. S1 of the Supplemental Material [44]. At 1 atm, TiH and TiH₂ are preferred stable phases, while other stoichiometries are energetically unstable against the elemental decomposition [Fig. 1(a)]. At the low pressure of 50 GPa, the stoichiometries

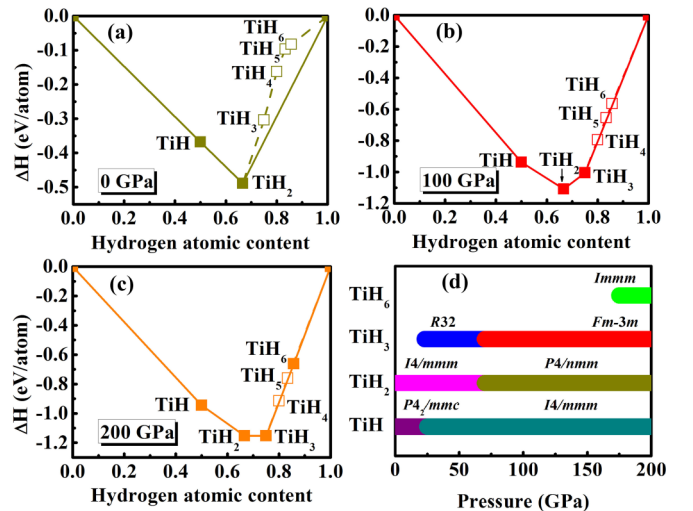


FIG. 1. (a)–(c) Calculated formation enthalpies of various titanium hydrides at 0, 100, and 200 GPa. The enthalpies are shown relative to the ground states of Ti and solid H₂ at corresponding pressure. Solid symbols located on the convex hull represent stable stoichiometries against any type of decomposition. (d) Pressure ranges in which the corresponding structures of different stoichiometries of Ti-H compounds are stable.

of TiH, TiH₂, and TiH₃ are stable, and this situation preserves up to 150 GPa (Fig. S1 of Supplemental Material [44]). Further comparison of energy for TiH₃ and 1/2 (H₂) + TiH₂ indicates that TiH₃ becomes energetically favored over elemental dissociation at about 25 GPa (Fig. S2(a) of Supplemental Material [44]). At 200 GPa, in addition to these three species, another stable stoichiometry of TiH₆ appears in the H-rich regime [Fig. 1(c)]. Upon comparing Fig. 1 here and Fig. S2(b) of the Supplemental Material [44], TiH₆ is found to be stable in the pressure range of 175–200 GPa. As is known, zero-point energy (ZPE) plays an important role in determining the stability of hydrogen-rich compounds. Therefore, we have recomputed the formation enthalpies of different Ti-H stoichiometries at 200 GPa with the inclusion of ZPE by using Eq. (9). As can be seen from Fig. S1(c) of the Supplemental Material [44], the convex hull remains essentially unchanged, and the stoichiometries of TiH, TiH₂, TiH₃, and TiH₆ are still stable at 200 GPa.

The pressure-phase diagram of the predicted titanium hydrides in 0–200 GPa is summarized and displayed in Fig. 1(d). The TiH stoichiometry is thermodynamically stable, covering the studied pressure range. *P4*₂/*mmc* is the stable form of TiH at ambient pressure; then it transforms into *I4/mmm* at 25 GPa. The conventional cell of tetragonal *I4/mmm* is depicted in Fig. 2(a). Ti and H atoms occupy the crystallographic *2a* and *2b* positions, and their site symmetries are both *4/mmm*. As for TiH₂, the centered tetragonal structure with space group *I4/mmm* (Fig. S3(a) of Supplemental Material [44]) transforms to the simple tetragonal *P4/nmm* structure at about 70 GPa, and the phase transition is in good agreement with previous experimental and theoretical works [30,31]. When titanium is threefold coordinated by H atoms, the structure possessing the rhombohedral *R32* is found to transform into face-centered-cubic *Fm-3m* [Fig. 2(b)] at about 70 GPa. For the most H-rich TiH₆ stoichiometry, it stabilizes above 175 GPa and crystalizes in an *Immm* structure [Fig. 2(c)]. Ti atoms occupy the crystallographic *4g* position (site symmetry is *m2m*), while two H atoms allocate *8n* positions (site symmetry is *..m*), and the other two H atoms allocate *4e* (site symmetry is *2mm*) and *4f* (site symmetry is *2mm*) positions. The lattice parameters

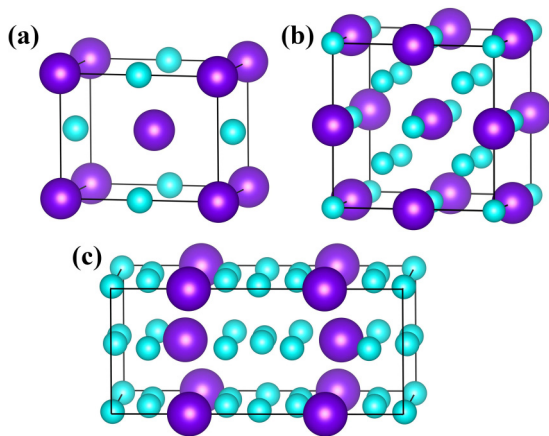


FIG. 2. Stable structures of Ti-H compounds at 200 GPa. (a) TiH in *I4/mmm* structure, (b) TiH₃ in *Fm-3m* structure, and (c) TiH₆ in *Immm* structure. Purple and blue spheres depict Ti and H atoms, respectively.

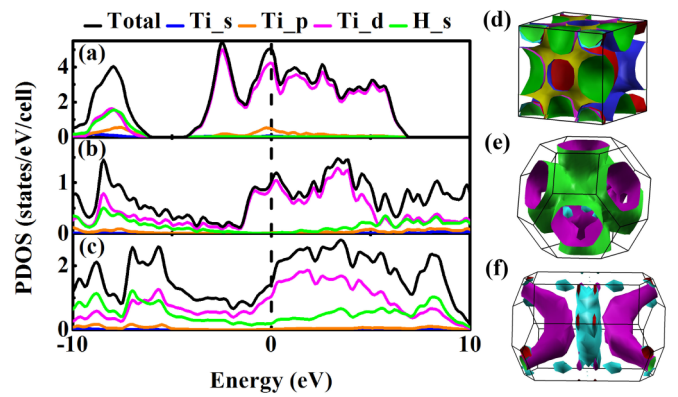


FIG. 3. The electronic density of states (DOS) and Fermi surfaces of titanium hydrides at 200 GPa. (a),(d) TiH in *I4/mmm* structure; (b),(e) TiH₃ in *Fm-3m* structure; and (c),(f) TiH₆ in *Immm* structure.

and atomic positions of uncovered Ti-H compounds are listed in Table S1 of the Supplemental Material [44].

The projected density of states (PDOS) and three-dimensional Fermi surfaces of *I4/mmm* (TiH), *I4/mmm* (TiH₂), *P4/nmm* (TiH₂), *Fm-3m* (TiH₃), and *Immm* (TiH₆) are calculated and depicted in Fig. 3 and in Fig. S4 of the Supplemental Material [44]. The finite density of states at the Fermi level [$N(\epsilon_F)$] and the complex Fermi surfaces reveal the metallic feature of all five structures. Apparently, the Ti-3*d* orbital dominates the $N(\epsilon_F)$, whereas the other states (i.e., H-1*s*, Ti-4*s*, Ti-4*p*) almost vanish near the Fermi level. Analyses of the bonding feature via the electron localization function (ELF, Figs. S5 and S6 of Supplemental Material [44]) and Bader charge analysis (Table S2 of Supplemental Material [44]) indicates the ionic nature of Ti-H with the charge transferred from Ti to H [45,46]. Moreover, the quasimolecular H₂ with the H-H separation ~ 0.86 Å is present in *Immm* (TiH₆) (Figs. S6(c), S6(d), and Table S3 of Supplemental Material [44]). The longer H-H distances than that (0.75 Å) in a free H₂ molecule [47] are attributed to the electrons transferring from Ti to H, which resides in the H₂ antibonding orbital and thus lengthens the intramolecular bond [27].

We then perform phonon and electron-phonon coupling (EPC) calculations for the species of TiH, TiH₂, TiH₃, and TiH₆ to investigate their potential superconductivity. As shown in Figs. S7 and S8 of the Supplemental Material [44], the absence of any imaginary vibrational mode in the whole Brillouin zone indicates the dynamical stability of the above phases. For all structures, the low-energy phonon modes are associated with Ti atoms, while the higher-frequency modes mainly correspond to the vibration of H atoms. The calculated EPC parameter λ for TiH, TiH₂, TiH₃, and TiH₆ at 200 GPa is 0.85, 0.27, 0.44, and 1.21, respectively. Figures S8 and S9 of the Supplemental Material [44] show the projected phonon density of states (PHDOS), Eliashberg spectral function $\alpha^2 F(\omega)$, and the electron-phonon integral $\lambda(\omega)$ at 200 GPa. Interestingly, the contribution from the H atoms to the total λ gradually increases in the order of *I4/mmm* (TiH) (3%) < *Fm-3m* (TiH₃) (14%) < *P4/nmm* (TiH₂) (17%) < *Immm* (TiH₆) (50%). For *I4/mmm* (TiH), *P4/nmm* (TiH₂), and *Fm-3m* (TiH₃), λ is considered to be dominated by the element frequency modes of the Ti atoms, while in *Immm* (TiH₆), midfrequency H-derived

phonons and low-frequency vibrations from the Ti atoms are both responsible for the EPC. The superconducting T_c can be evaluated by utilizing Eq. (1). Using the calculated logarithmic average frequency ω_{\log} , along with the Coulomb pseudopotential μ^* value of 0.1 and 0.13 [9], the resultant T_c values are 9.7–11.8 K, 0–0.1 K, 1.8–3.5 K, and 69.0–77.8 K for TiH, TiH₂, TiH₃, and TiH₆, respectively, at 200 GPa. Values of T_c , ω_{\log} , λ are listed in Table S4 of the Supplemental Material [44]. The strong EPC ($\lambda = 1.21$) and high ω_{\log} (858 K) in TiH₆ lead to its higher T_c than the cases in the other three compounds.

It is arresting that the T_c of TiH₃ is only several Kelvin though it crystallizes in the highly symmetrical $Fm\bar{3}m$ and possesses the same stoichiometry as the high- T_c cubic SH₃ [16]. Moreover, an analogous feature has also been predicted in the $Fm\bar{3}m$ (VH₃) [29]. We then perform the analysis on the low critical temperature in TiH₃ and VH₃ as compared to the high- T_c SH₃ and the medium- T_c SeH₃. The calculated T_c , λ , and ω_{\log} at 200 GPa are listed in Table I. As is apparent, the larger EPC λ (2.25) and ω_{\log} (1320 K) lead to the high T_c of SH₃. Strikingly, λ in SH₃ is about two times as that in SeH₃, and five times as the ones in TiH₃ and VH₃. To gain insight into the mechanism of contrasting electron-phonon coupling between TiH₃, VH₃, SH₃, and SeH₃, we extend the calculations in two aspects. On one hand, the equation defined in McMillan's strong-coupling theory is adopted [33],

$$\lambda = \frac{\eta}{M\langle\omega^2\rangle} = \frac{N(\varepsilon_F)\langle I^2\rangle}{M\langle\omega^2\rangle}, \quad (10)$$

where M is the atomic mass, $N(\varepsilon_F)$ is for a single spin (i.e. one-half of the value shown in Fig. 3, which is for

both spins), and $\langle I^2\rangle$ is the average over the Fermi surface of the electron-phonon matrix element. Values for $\langle I^2\rangle$ are obtained indirectly using Eq. (10) from the calculated values of λ , $N(\varepsilon_F)$, and the average phonon frequency $\langle\omega^2\rangle^{1/2}$, as given in Table I. For cubic VH₃ and TiH₃, λ is suppressed by an extremely low $\langle I^2\rangle$, though the higher $N(\varepsilon_F)$ and lower $\langle\omega^2\rangle^{1/2}$ play a more positive role in enhancing λ than the case in SH₃. Therefore, the tremendous difference of λ in the four compounds is attributed to the enormous disparity of the average electron-phonon matrix element $\langle I^2\rangle$. As for SeH₃, λ is restricted by the higher M and $\langle\omega^2\rangle^{1/2}$, though $\langle I^2\rangle$ is similar to that in SH₃.

On the other hand, we evaluate the electron-phonon contribution to the phonon linewidths as defined in Eq. (6). The phonon spectra, phonon density of states, Eliashberg phonon spectral function $\alpha^2F(\omega)$, and the electron-phonon integral λ of $M\text{H}_3$ ($M = \text{S, Ti, V, Se}$) are depicted in Fig. 4. Obviously, in TiH₃ and VH₃, the phonon linewidths ($\gamma_{\mathbf{q}\nu}$) of all branches are fairly uniform throughout the spectrum and much smaller than the scale of phonon linewidths in SH₃ and SeH₃ (see Fig. 4 and see Table S5 of Supplemental Material [44]). The electron-phonon coupling at a given phonon momentum \mathbf{q} for a phonon mode ν can be obtain from Eq. (8). For TiH₃ and VH₃, the puny $\gamma_{\mathbf{q}\nu}$ resulted in the weak EPC. Meanwhile, the $\omega_{\mathbf{q}\nu}$ is a negative factor of $\lambda_{\mathbf{q}\nu}$, so the high-frequency phonon modes contribute little to $\lambda_{\mathbf{q}\nu}$ with the fact that $\gamma_{\mathbf{q}\nu}$ at all branches are almost equal. Thus, the optical modes seldom contribute to the total λ . The integrated λ in Fig. 4 (right subpanels) show that the optical modes contribute only 14% and 18% to the EPC λ in TiH₃ and VH₃, and the acoustic branches dominate

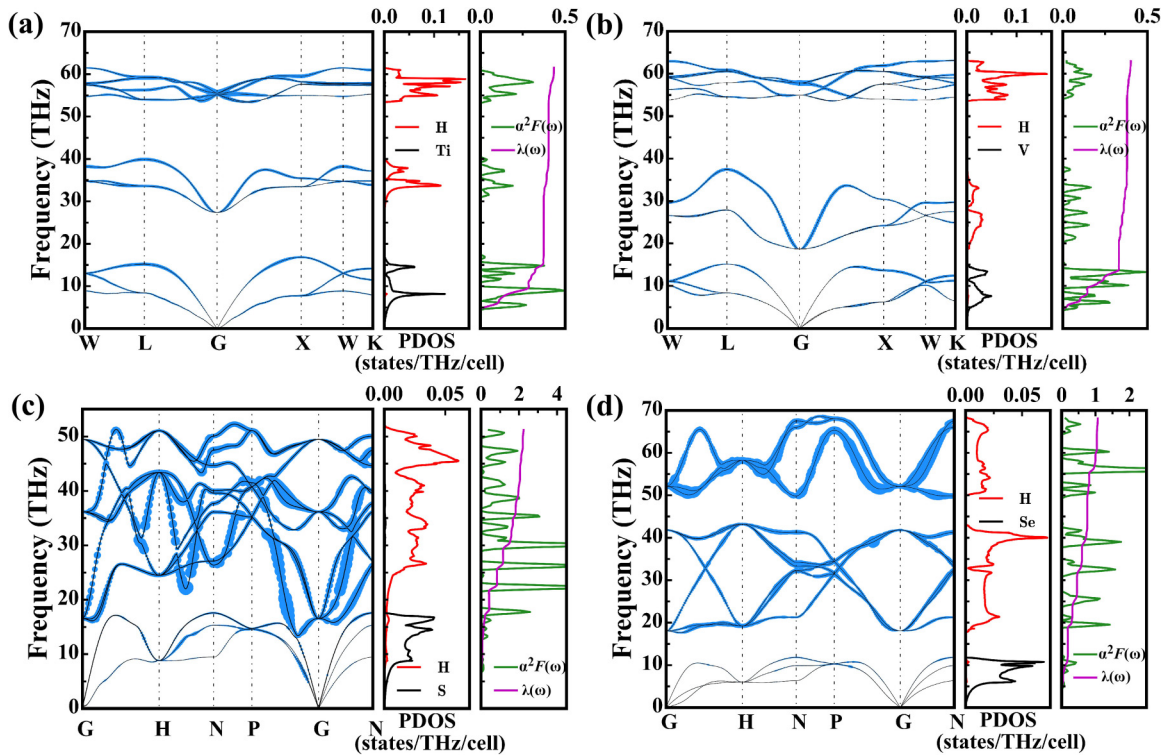


FIG. 4. Phonon spectra, phonon density of states, Eliashberg phonon spectral function $\alpha^2F(\omega)$, and the electron-phonon integral λ of (a) $Fm\bar{3}m$ (TiH₃), (b) $Fm\bar{3}m$ (VH₃), (c) $Im\bar{3}m$ (SH₃), and (d) $Im\bar{3}m$ (SeH₃) at 200 GPa. The magnitude of the phonon linewidths is illustrated by the size of the blue circles.

TABLE I. The calculated electronic density of states at the Fermi level $N(\varepsilon_F)$ (states/spin/eV/cell), the logarithmic average phonon frequency ω_{\log} (K), the average phonon frequency $\langle\omega^2\rangle^{1/2}$ (THz), the average electron-phonon matrix element $\langle I^2 \rangle$ (eV/Å)², electron-phonon coupling parameters λ , and superconducting critical temperatures T_c (K) for different compounds at 200 GPa.

Phases	$N(\varepsilon_F)$	ω_{\log}	$\langle\omega^2\rangle^{1/2}$	$\langle I^2 \rangle$	λ	T_c
<i>Fm-3m</i> (TiH ₃)	0.52	532	126	1.83	0.44	1.8–3.5
<i>Fm-3m</i> (VH ₃)	0.39	567	121	2.09	0.40	1.1–2.5
<i>Im-3m</i> (SH ₃)	0.25	1320	187	44.43	2.25	192.2–204.6
<i>Im-3m</i> (SeH ₃)	0.23	1423	241	37.44	1.07	95.1–109.4

the electron-phonon coupling. As for SH₃ and SeH₃, the huge γ_{qv} of the optical branches generate the strong EPC, and the optical branches contribute 81% and 83% to the integrated EPC parameter λ . It is worth mentioning that the smaller λ of SeH₃ than the one of SH₃ is attributed to the higher phonon frequency and atomic mass in SeH₃, though the γ_{qv} in them are similar. In general, the enormous difference of EPC in the four compounds is ascribed to the disparate contribution from optical modes, which can be reflected by the contrasting phonon linewidths.

As a positive contributor to EPC λ [Eq. (8)], the phonon linewidths γ_{qv} are mainly affected by two factors [Eq. (6)]: the electron-phonon matrix element $g_{mn}^v(\mathbf{k}, \mathbf{q})$ and the nesting function. The nesting function is defined as

$$\xi_{\mathbf{q}} = \sum_{mn} \sum_{\mathbf{k}} \delta(\varepsilon_{m,\mathbf{k}+\mathbf{q}} - \varepsilon_F) \times \delta(\varepsilon_{n,\mathbf{k}} - \varepsilon_F), \quad (11)$$

and describes the probability of phase space for scattering across the Fermi surface. For the G point, the maximum value of $\xi_{\mathbf{q}}$ can serve as a good measure of the degree of metallization [48]; the nesting at other \mathbf{q} points means the positive contribution from electrons to the formation of the Cooper pair. And the large value of $\xi_{\mathbf{q}}$ will boost the EPC strength. Figure 5 depicts the $\xi_{\mathbf{q}}$ along the high-symmetry lines of TiH₃, VH₃, SH₃, and SeH₃. At the G point, the maximum value of $\xi_{\mathbf{q}}$ in SH₃ and SeH₃ is a little higher than that in TiH₃ and VH₃, demonstrating the tallish degree of metallization in SH₃ and SeH₃. As for the high-symmetry points in the Brillouin zone, the $\xi_{\mathbf{q}}$ of SH₃ and SeH₃ is approximately accordant with the case in TiH₃ and VH₃, indicating that nesting functions contribute analogously to the phonon linewidths γ_{qv} in the four compounds, and the contributions from global electronic structures to the formation of the Cooper pair are similar. Thus, the large γ_{qv} of SH₃ and SeH₃ is attributed to the large $g_{mn}^v(\mathbf{k}, \mathbf{q})$ derived from optical modes, i.e., the intensity of scattering of electrons by optic phonons.

It has been reported that T_c in SH₃ reaches ~ 200 K at 200 GPa, and decreases nearly linearly with increasing pressure [16]. As for SeH₃, the weakly pressure-dependent superconducting T_c around 110 K was reported [26]. Therefore, the T_c in SH₃ and SeH₃ could be deemed as largest at 200 GPa, which is close to the pressures of structural transitions (~ 180 GPa in SH₃ and ~ 170 GPa in SeH₃). So, we have performed some further calculations for TiH₃ and VH₃ in the lower-pressure range in order to investigate whether they might have higher T_c nearer to their structural transitions. As shown in Table S6 of the Supplemental Material [44], TiH₃ and VH₃ have their maximum T_c at the lower pressures, which are nearer to their respective transitional pressures. The estimated

T_c values are 9.9–13.3 K and 8.4–11.1 K for TiH₃ at 80 GPa and VH₃ at 140 GPa, respectively. With increasing pressure, the phonon tends to harden (see phonon dispersions in Figs. 4(a) and 4(b) and in Fig. S10 of Supplemental Material [44]) and ω_{\log} raises, but the EPC parameter λ decreases (Table S6 of Supplemental Material [44]). According to Eq. (1), T_c are the balanced results of λ and ω_{\log} . The reduction of T_c in TiH₃ and VH₃ is dominated by the descending EPC λ . Then the declining tendency of λ is explored by Eq. (10). In TiH₃ and VH₃, the increasing $\langle I^2 \rangle$ with pressurization plays a positive role in enhancing EPC λ . However, the contributions from the descending $N(\varepsilon_F)$ and the increasing phonon frequencies are larger and result in the decrease of λ upon compression. We then performed the analyses of phonon linewidths γ_{qv} and the Fermi surface nesting function $\xi_{\mathbf{q}}$ in $M\text{H}_3$ ($M = \text{S}, \text{Ti}, \text{V}, \text{Se}$) at the pressures corresponding to their respective maximum T_c . The γ_{qv} and $\xi_{\mathbf{q}}$ for TiH₃ at 80 GPa and VH₃ at 140 GPa are calculated and displayed in Figs. S10 and S11 of the Supplemental Material [44]. As shown in Fig. S11 of the Supplemental Material [44], $\xi_{\mathbf{q}}$ for TiH₃ and VH₃ at lower pressures are approximately accordant with the cases at 200 GPa, and thus are analogous to the case of SH₃ and SeH₃ [Figs. 5(c) and 5(d)]. Comparing the γ_{qv} in TiH₃ and VH₃ at lower pressures (Fig. S10 of Supplemental Material [44]) with the cases in SH₃ and SeH₃ at 200 GPa [Figs. 4(c) and 4(d)], we can find that the large γ_{qv} of SH₃ and SeH₃ is attributed to the large $g_{mn}^v(\mathbf{k}, \mathbf{q})$ derived from optical modes, which is in accordance with the above discussions.

It is also worth mentioning that the hydrogen states are far away from the Fermi level in the low- T_c TiH₃ [Fig. 3(b)] and VH₃ [29]. As for SH₃ and SeH₃, large H-derived electronic density of states at the Fermi level is observed [16,26]. Therefore, we have compared the electronic density of states (DOS) in TiH₃, VH₃, SH₃, and SeH₃ at 200 GPa, as shown in Fig. S12 of the Supplemental Material [44]. From the aspect of partial DOS, the contribution from H to the electronic density of states at the Fermi level [$N(\varepsilon_F)$] in SH₃ and SeH₃ is higher than the cases in TiH₃ and VH₃. The large H-derived electronic density of states at the Fermi level is beneficial for strong EPC λ in SH₃ and SeH₃. Generally speaking, $N(\varepsilon_F)$ indicates all of the candidate electrons to form Cooper pairs. It is clear that the large $N(\varepsilon_F)$ plays a positive role in enhancing the EPC λ . In terms of Eqs. (6), (7), and (11), the nesting function $\xi_{\mathbf{q}}$ ultimately determines the probability of the candidate electrons participating in the forming of Cooper pairs in each \mathbf{q} point in the Brillouin zone. The contribution from the global electronic structure to EPC λ is reflected in the summation of $\xi_{\mathbf{q}}$ at all the \mathbf{q} points in the Brillouin zone. As discussed above, the

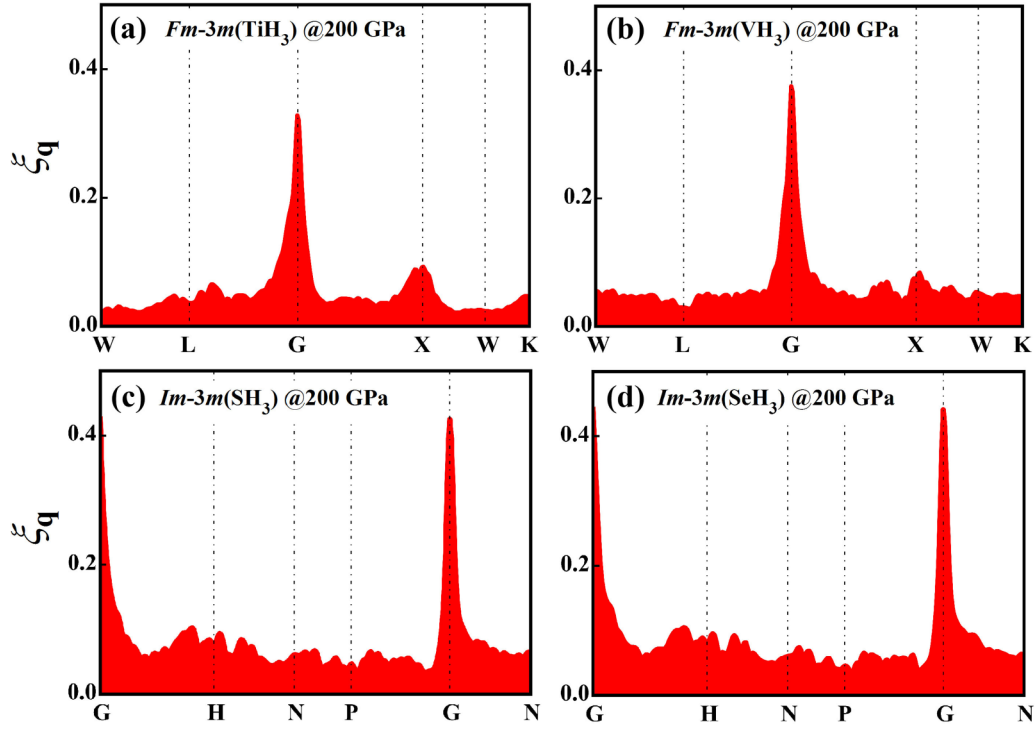


FIG. 5. The calculated nesting function $\xi_{\mathbf{q}}$ along some special \mathbf{q} trajectories for (a) $Fm-3m$ (TiH_3), (b) $Fm-3m$ (VH_3), (c) $Im-3m$ (SH_3), and (d) $Im-3m$ (SeH_3) at 200 GPa. The present calculations employ 1 139 103, 1 139 103, 1 065 015, and 1 046 493 $k + \mathbf{q}$ points for the four compounds to attain their respective energy eigenvalues.

$\xi_{\mathbf{q}}$ contribute analogously to the phonon linewidths $\gamma_{\mathbf{q}\nu}$ in the four compounds, and the contributions from global electronic structures to the EPC λ are similar. The contrasting EPC λ in MH_3 ($M = S, Ti, V, Se$) is mainly attributed to the disparate intensity of electrons interacting with optic phonons, rather than the contributions from global electronic structures.

From Fig. 4, we can find that the optical phonon frequencies (ω_{Opt}) in SH_3 and SeH_3 vary greatly with different wave vector \mathbf{q} in the Brillouin zone, which discloses the strong dependency of ω_{Opt} on \mathbf{q} , and compared to the independent frequency with \mathbf{q} in the Einstein model [49,50], while in TiH_3 and VH_3 , the dependency relationship between frequency and \mathbf{q} can be described by the Einstein model. The dependency of ω_{Opt} on \mathbf{q} can be measured by the formula expressed as

$$\sigma_{\text{Freq}} = \frac{1}{N_{\mathbf{q}}} \sum_{\mathbf{q}\nu} \sqrt{(\omega_{\mathbf{q}\nu} - \mu_{\nu})^2}, \quad (12)$$

where $\omega_{\mathbf{q}\nu}$ indicates the phonon frequency at wave vector \mathbf{q} with mode ν , μ_{ν} is the average frequency of mode ν , and $N_{\mathbf{q}}$ represents the number of \mathbf{q} points in the Brillouin zone. Large value of σ_{OptFreq} means ω_{Opt} strongly depends on \mathbf{q} , while the small value signifies the relative weak dependency relationship. The values are 2.0 for SH_3 , 2.4 for SeH_3 , 0.9 for TiH_3 , and 1.1 for VH_3 , respectively. Obviously, σ_{OptFreq} in SH_3 and SeH_3 are about two times that in TiH_3 and VH_3 . The optical phonons with larger σ_{OptFreq} provide a wider range of energy from various vibrational modes, which enhance the probability of satisfying the formation energy of Cooper pairs and would be beneficial to high T_c . A similar feature can also be found in the reported high- T_c cubic hydrides, such as SiH_3 [14], MgH_6 [51], CaH_6 [12], and YH_6 [22].

In the four compounds investigated here, the contributions from global electronic structures to EPC λ are similar. In TiH_3 and VH_3 , the intensity of EPC is suppressed by the puny $g_{mn}^v(\mathbf{k}, \mathbf{q})$ originated from the optical branches. As for SeH_3 and SH_3 , the larger σ_{OptFreq} promote the intensity of scattering of the electrons by optic phonon modes, and then induce stronger EPC. The EPC λ in SeH_3 is restrained by the higher phonon frequency and larger atomic mass than that of SH_3 . These results disclose the superconductive character in MH_3 ($M = S, Ti, V, Se$), which is dominated by the intensity of the scattering of electrons by optic phonons. Moreover, the feature that ω_{Opt} strongly depends on \mathbf{q} will be beneficial to high-temperature superconductivity.

IV. CONCLUSIONS

In conclusion, the ground-state phases and properties of the Ti-H system under high pressures have been extensively explored by utilizing an evolutionary local random structural prediction method combined with first-principles calculations. The species of TiH and TiH_2 are found to be stable over the explored pressure range, and the other stoichiometries become thermodynamically stable upon compression, beyond 25 GPa for TiH_3 and 175 GPa for TiH_6 . Moreover, the structures and phase transition in TiH_2 are in good agreement with the previous experimental and theoretical works. The electronic properties of TiH , TiH_2 , TiH_3 , and TiH_6 show that they are all metallic at 200 GPa. Further electron-phonon coupling calculations reveal the potential superconductivity in $I4/mmm$ (TiH), $P4/nmm$ (TiH_2), $Fm-3m$ (TiH_3), and $Immm$ (TiH_6) with estimated T_c of 9.7–11.8 K, 0–0.1 K, 1.8–3.5 K, and

69.0–77.8 K at the pressure of 200 GPa. Conspicuously, the low T_c in TiH_3 (~ 4 K) contrast sharply with the high T_c (above 200 K) in SH_3 , though they both possess the same stoichiometry and both crystallize in high-symmetrical cubic crystal. Then we progress to the comparison of superconductivity in cubic SH_3 , TiH_3 , and SeH_3 , along with the low- T_c VH_3 that we investigated before. As is expected, the tremendous difference of T_c is attributed to the distinguishing EPC parameter λ . By analyzing phonon linewidths and the Fermi surface nesting function, we ascribe the contrasting EPC parameter λ to the disparate intensity of the scattering of electrons by optic phonon modes, rather than the contributions from global electronic structures. Furthermore, the feature that ω_{Opt} strongly depends on \mathbf{q} might be an essential ingredient for strong EPC λ and high T_c .

ACKNOWLEDGMENTS

This work was supported by the National Natural Science Foundation of China (Grants No. 51632002, No. 51572108, No. 11634004, No. 11174102, and No. 11774119), Program for Changjiang Scholars and Innovative Research Team in University (Grant No. IRT_15R23), National Found for Fostering Talents of basic Science (Grant No. J1103202), National Key Research and Development Program of China (under Grant No. 2016YFB0201204), the Development Program of Science and Technology of Jilin Province, China (Grant No. 20150312002ZG), the 111 Project (Grant No. B12011), and Graduate Innovation Fund of Jilin University (Grant No. 2016016). Parts of the calculations were performed in the High Performance Computing Center (HPCC) of Jilin University.

-
- [1] N. W. Ashcroft, *Phys. Rev. Lett.* **21**, 1748 (1968).
 [2] J. M. McMahon and D. M. Ceperley, *Phys. Rev. B* **85**, 219902(E) (2012).
 [3] T. Ishikawa, H. Nagara, T. Oda, N. Suzuki, and K. Shimizu, *Phys. Rev. B* **90**, 104102 (2014).
 [4] M. Borinaga, I. Errea, M. Calandra, F. Mauri, and A. Bergara, *Phys. Rev. B* **93**, 174308 (2016).
 [5] P. Dalladay-Simpson, R. T. Howie, and E. Gregoryanz, *Nature (London)* **529**, 63 (2016).
 [6] R. P. Dias and I. F. Silvera, *Science* **355**, 715 (2017).
 [7] A. F. Goncharov and V. V. Struzhkin, *Science* **357**, eaam9736 (2017).
 [8] X. D. Liu, P. Dalladay-Impson, R. T. Howie, B. Li, and E. Gregoryanz, *Science* **357**, eaan2286 (2017).
 [9] N. W. Ashcroft, *Phys. Rev. Lett.* **92**, 187002 (2004).
 [10] H. Zhang, X. Jin, Y. Lv, Q. Zhuang, Y. Liu, Q. Lv, K. Bao, D. Li, B. Liu, and T. Cui, *Sci. Rep.* **5**, 8845 (2015).
 [11] H. Zhang, X. Jin, Y. Lv, Q. Zhuang, Y. Liu, Q. Lv, K. Bao, D. Li, B. Liu, and T. Cui, *RSC Adv.* **5**, 107637 (2015).
 [12] H. Wang, J. S. Tse, K. Tanaka, T. Iitaka, and Y. Ma, *Proc. Natl. Acad. Sci. USA* **109**, 6463 (2012).
 [13] Y. Liu, D. Duan, F. Tian, H. Liu, C. Wang, X. Huang, D. Li, Y. Ma, B. Liu, and T. Cui, *Inorg. Chem.* **54**, 9924 (2015).
 [14] X. Jin, X. Meng, Z. He, Y. Ma, B. Liu, T. Cui, G. Zou, and H. K. Mao, *Proc. Natl. Acad. Sci. USA* **107**, 9969 (2010).
 [15] D. Zhou, X. Jin, X. Meng, G. Bao, Y. Ma, B. Liu, and T. Cui, *Phys. Rev. B* **86**, 014118 (2012).
 [16] D. Duan, Y. Liu, F. Tian, D. Li, X. Huang, Z. Zhao, H. Yu, B. Liu, W. Tian, and T. Cui, *Sci. Rep.* **4**, 6968 (2014).
 [17] A. P. Drozdov, M. I. Erements, I. A. Troyan, V. Ksenofontov, and S. I. Shylin, *Nature (London)* **525**, 73 (2015).
 [18] D. Duan, X. Huang, F. Tian, D. Li, H. Yu, Y. Liu, Y. Ma, B. Liu, and T. Cui, *Phys. Rev. B* **91**, 180502(R) (2015).
 [19] I. Errea, M. Calandra, C. J. Pickard, J. Nelson, R. J. Needs, Y. Li, H. Liu, Y. Zhang, Y. Ma, and F. Mauri, *Phys. Rev. Lett.* **114**, 157004 (2015).
 [20] N. Bernstein, C. S. Hellberg, M. D. Johannes, I. I. Mazin, and M. J. Mehl, *Phys. Rev. B* **91**, 060511(R) (2015).
 [21] M. Einaga, M. Sakata, T. Ishikawa, K. Shimizu, M. I. Erements, A. P. Drozdov, I. A. Troyan, N. Hirao, and Y. Ohishi, *Nat. Phys.* **12**, 835 (2016).
 [22] Y. Li, J. Hao, H. Liu, J. S. Tse, Y. Wang, and Y. Ma, *Sci. Rep.* **5**, 9948 (2015).
 [23] H. Liu, I. I. Naumov, R. Hoffmann, N. W. Ashcroft, and R. J. Hemley, *Proc. Natl. Acad. Sci. USA* **114**, 6990 (2017).
 [24] F. Peng, Y. Sun, C. J. Pickard, R. J. Needs, Q. Wu, and Y. Ma, *Phys. Rev. Lett.* **119**, 107001 (2017).
 [25] Q. Zhuang, X. Jin, T. Cui, Y. Ma, Q. Lv, Y. Li, H. Zhang, X. Meng, and K. Bao, *Inorg. Chem.* **56**, 3901 (2017).
 [26] S. Zhang, Y. Wang, J. Zhang, H. Liu, X. Zhong, H. F. Song, G. Yang, L. Zhang, and Y. Ma, *Sci. Rep.* **5**, 15433 (2015).
 [27] X. Zhong, H. Wang, J. Zhang, H. Liu, S. Zhang, H. F. Song, G. Yang, L. Zhang, and Y. Ma, *Phys. Rev. Lett.* **116**, 057002 (2016).
 [28] Y. Ma, D. Duan, Z. Shao, H. Yu, H. Liu, F. Tian, X. Huang, D. Li, B. Liu, and T. Cui, *Phys. Rev. B* **96**, 144518 (2017).
 [29] Q. Zhuang, X. Jin, Q. Lv, Y. Li, Z. Shao, Z. Liu, X. Li, H. Zhang, X. Meng, K. Bao, and T. Cui, *Phys. Chem. Chem. Phys.* **19**, 26280 (2017).
 [30] P. E. Kalita, S. V. Sinogeikin, K. Lipinska-Kalita, T. Hartmann, X. Ke, C. Chen, and A. Cornelius, *J. Appl. Phys.* **108**, 043511 (2010).
 [31] G. Gao, A. Bergara, G. Liu, and Y. Ma, *J. Appl. Phys.* **113**, 103512 (2013).
 [32] K. V. Shanavas, L. Lindsay, and D. S. Parker, *Sci. Rep.* **6**, 28102 (2016).
 [33] W. L. McMillan, *Phys. Rev.* **167**, 331 (1968).
 [34] P. B. Allen and R. C. Dynes, *Phys. Rev. B* **12**, 905 (1975).
 [35] P. Morel and P. W. Anderson, *Phys. Rev.* **125**, 1263 (1962).
 [36] K. T. Chan, B. D. Malone, and M. L. Cohen, *Phys. Rev. B* **88**, 064517 (2013).
 [37] P. B. Allen, *Phys. Rev. B* **6**, 2577 (1972).
 [38] K. T. Chan, B. D. Malone, and M. L. Cohen, *Phys. Rev. B* **86**, 094515 (2012).
 [39] Y. Li, X. Jin, T. Cui, Q. Zhuang, Q. Lv, G. Wu, X. Meng, K. Bao, B. Liu, and Q. Zhou, *RSC Adv.* **7**, 7424 (2017).
 [40] J. P. Perdew, K. Burke, and M. Ernzerhof, *Phys. Rev. Lett.* **77**, 3865 (1996).
 [41] G. Kresse and J. Furthmüller, *Phys. Rev. B* **54**, 11169 (1996).
 [42] P. Giannozzi, S. Baroni, N. Bonini, M. Calandra, R. Car, C. Cavazzoni, D. Ceresoli, G. L. Chiarotti, M. Cococcioni, I. Dabo, A. Dal Corso, S. de Gironcoli, S. Fabris, G. Fratesi, R. Gebauer, U. Gerstmann, C. Gougoussis, A. Kokalj, M. Lazzeri,

- L. Martin-Samos, N. Marzari, F. Mauri, R. Mazzarello, S. Paolini, A. Pasquarello, L. Paulatto, C. Sbraccia, S. Scandolo, G. Sciauzero, A. P. Seitsonen, A. Smogunov, P. Umari, and R. M. Wentzcovitch, *J. Phys.: Condens. Matter* **21**, 395502 (2009).
- [43] N. Troullier and J. L. Martins, *Phys. Rev. B* **43**, 1993 (1991).
- [44] See Supplemental Material at <http://link.aps.org/supplemental/10.1103/PhysRevB.98.024514> for the calculated formation enthalpies, electronic properties, phonon dispersions, electron-phonon coupling features of titanium hydrides; the electron-phonon coupling features of TiH₃ and VH₃ at lower pressures.
- [45] A. D. Becke and K. E. Edgecombe, *J. Chem. Phys.* **92**, 5397 (1990).
- [46] J. K. Burdett and T. A. McCormick, *J. Phys. Chem. A* **102**, 6366 (1998).
- [47] V. Labet, P. Gonzalez-Morelos, R. Hoffmann, and N. W. Ashcroft, *J. Chem. Phys.* **136**, 074501 (2012).
- [48] X. Jin, X. J. Chen, T. Cui, H. K. Mao, H. Zhang, Q. Zhuang, K. Bao, D. Zhou, B. Liu, Q. Zhou, and Z. He, *Proc. Natl. Acad. Sci. USA* **113**, 2366 (2016).
- [49] J. L. Fleche, *Phys. Rev. B* **65**, 245116 (2002).
- [50] A. Otero-de-la Roza, D. Abbasi-Pérez, and V. Luaña, *Comput. Phys. Commun.* **182**, 2232 (2011).
- [51] X. Feng, J. Zhang, G. Gao, H. Liu, and H. Wang, *RSC Adv.* **5**, 59292 (2015).